

# First-principles calculation of lattice thermal conductivities of $\alpha$ -, $\beta$ -, and $\gamma$ - $\text{Si}_3\text{N}_4$

Kazuyoshi Tatsumi,<sup>1,2,\*</sup> Atsushi Togo,<sup>2</sup> and Isao Tanaka<sup>2,3,4</sup>

<sup>1</sup>*Institute of Materials and Systems for Sustainability,  
Nagoya University, Chikusa, Nagoya 464-8603, Japan*

<sup>2</sup>*Center for Elements Strategy Initiative for Structural Materials,  
Kyoto University, Sakyo, Kyoto 606-8501, Japan*

<sup>3</sup>*Department of Materials Science and Engineering,  
Kyoto University, Sakyo, Kyoto 606-8501, Japan*

<sup>4</sup>*Nanostructures Research Laboratory, Japan Fine Ceramics Center, Atsuta, Nagoya 456-8587, Japan*

Lattice thermal conductivities of  $\alpha$ -,  $\beta$ - and  $\gamma$ - $\text{Si}_3\text{N}_4$  phases are investigated from *ab-initio* anharmonic lattice dynamics, within the single-mode relaxation-time approximation of the linearized phonon Boltzmann transport equation. At 300 K, the lattice thermal conductivity of  $\beta$ - $\text{Si}_3\text{N}_4$  is calculated as  $\kappa_{xx} = 73$  and  $\kappa_{zz} = 199$  (in units of  $\text{Wm}^{-1}\text{K}^{-1}$ ), that is consistent with the reported experimental values of 69 and 180, respectively. For  $\alpha$ - $\text{Si}_3\text{N}_4$ ,  $\kappa_{xx} = 68$  and  $\kappa_{zz} = 100$  are obtained. The difference of anisotropy between these phases is originated from their characteristic difference in the phonon band structures, closely related to the crystal structures. In  $\alpha$ - $\text{Si}_3\text{N}_4$ , acoustic-mode phonons below 6 THz are the main heat carriers. In  $\beta$ - $\text{Si}_3\text{N}_4$ , the phonon modes up to 12 THz contribute to the lattice thermal conductivity. In  $\gamma$ - $\text{Si}_3\text{N}_4$ ,  $\kappa = 77$  is obtained. The distribution of phonon mode contributions to lattice thermal conductivity with respect to phonon frequency is found to closely resemble that for  $\kappa_{xx}$  of  $\beta$ - $\text{Si}_3\text{N}_4$  although the phonon lifetimes of  $\gamma$ - $\text{Si}_3\text{N}_4$  are twice shorter than those of  $\beta$ - $\text{Si}_3\text{N}_4$ .

## I. INTRODUCTION

Several nitride insulators are known to exhibit high thermal conductivities and are important for heat transfer materials at elevated temperatures. For example, Slack *et al.*<sup>1</sup> reported that wurtzite-type AlN has thermal conductivity exceeding  $100 \text{ Wm}^{-1}\text{K}^{-1}$ .  $\text{Si}_3\text{N}_4$  has become another promising thermal conductive insulator because its thermal conductivity has been improved up to  $177 \text{ Wm}^{-1}\text{K}^{-1}$  by using the advanced ceramic technologies related to the densification and microstructure control.<sup>2–5</sup> Since the  $\text{Si}_3\text{N}_4$  ceramics also exhibit high mechanical strength at elevated temperatures, they are regarded as ideal materials for the use in various applications, such as engine components, gas turbines, and heat sink substrates of power semiconductor devices.

At atmospheric pressure,  $\text{Si}_3\text{N}_4$  has two phases,  $\alpha$  and  $\beta$ , which are generally considered as low- and high-temperature phases, respectively.<sup>2,5,6</sup> Their crystal structures belong to the space groups of P31c and P6<sub>3</sub>/m, respectively.<sup>7,8</sup> These structures have different stacking manners of equivalent basal layer structures composed of  $\text{SiN}_4$  tetrahedra.<sup>9</sup> In Fig. 1 these layer structures are depicted from the principal axis direction. They are denoted as A, B, C, and D in the  $\alpha$  phase and A and B in the  $\beta$  phase, respectively. The stacking manners in  $\alpha$ - and  $\beta$ - $\text{Si}_3\text{N}_4$  are thus as ABCDABCD.. and ABAB.., respectively. The  $\alpha$  phase has additional two layer structures of C and D, which are related to A and B by the  $c$  glide operation.<sup>9</sup> Along this direction the lattice constant of the  $\alpha$  phase is approximately twice longer than that of the  $\beta$  phase.

The experimental thermal conductivities<sup>2–5,11</sup> of the  $\text{Si}_3\text{N}_4$  polymorphs were measured on the polycrystalline bulk samples. These values were significantly affected by

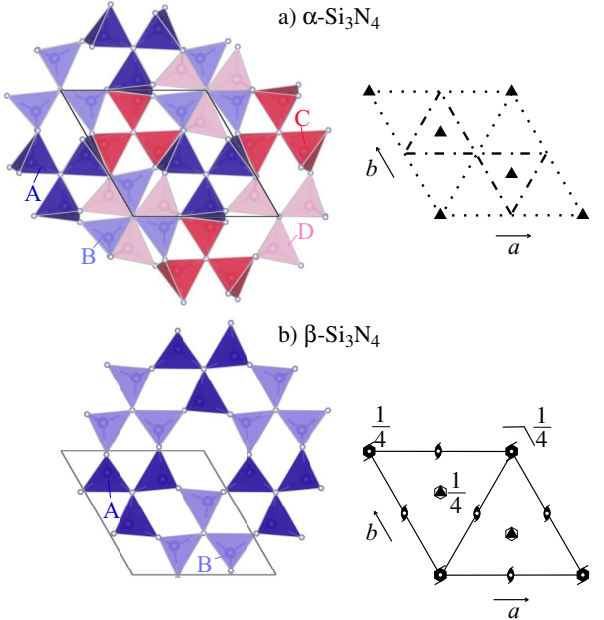


FIG. 1. (color online) Crystal structures of  $\alpha$ - and  $\beta$ - $\text{Si}_3\text{N}_4$ . Stacking of  $\text{SiN}_4$  tetrahedron layers are shown in left. (a) ABCDABCD.. for  $\alpha$ - $\text{Si}_3\text{N}_4$ . (b) ABAB.. for  $\beta$ - $\text{Si}_3\text{N}_4$ . Space group diagrams<sup>10</sup> in P31c ( $\alpha$ - $\text{Si}_3\text{N}_4$ ) and P6<sub>3</sub>/m ( $\beta$ - $\text{Si}_3\text{N}_4$ ) are shown in right.

the lattice defects, impurities, shapes and orientations of the constituent crystal grains;<sup>12</sup> the thermal conductivity intrinsic to defect-free  $\text{Si}_3\text{N}_4$  has not been established. As an experimental approach for it, Li *et al.*<sup>13</sup> applied the high-resolution thermoreflectance microscopy on single  $\beta$ - $\text{Si}_3\text{N}_4$  grains in a ceramic sample. Their analyzed thermal conductivity was 69 and  $180 \text{ Wm}^{-1}\text{K}^{-1}$  along

the  $a$  and  $c$  axes, respectively. These values respectively correspond to the  $xx$  and  $zz$  elements of the lattice thermal conductivity tensor  $\kappa$ . We consider the anisotropy of  $\kappa_{zz}/\kappa_{xx} \sim 3$  is relatively large. Theoretically, Hirosaki *et al.*<sup>12</sup> estimated the  $\kappa$  by applying the Green-Kubo formulation to the molecular dynamics (MD) method with the interatomic potentials proposed by Vashishta *et al.*<sup>14</sup>. They calculated  $\kappa_{xx}$  and  $\kappa_{zz}$  of  $\alpha\text{-Si}_3\text{N}_4$  as 105 and  $225 \text{ W m}^{-1}\text{K}^{-1}$ , and those of  $\beta\text{-Si}_3\text{N}_4$  as 170 and  $450 \text{ W m}^{-1}\text{K}^{-1}$ , respectively. The ratio  $\kappa_{zz}/\kappa_{xx}$  in  $\beta\text{-Si}_3\text{N}_4$  agreed well with the experimental ratio; the  $\kappa_{xx}$  and  $\kappa_{zz}$  overestimated the experimental  $\kappa$  more than twice.

Based on a first principles calculation and Boltzmann transport theory<sup>15</sup>, Togo *et al.* recently calculated  $\kappa$  of many polymorphs of the zincblende- and wurtzite-type structures. Their crystal structures have stacking orders of the densest atom planes as ABCABC.. and ABAB.., respectively. The different stacking orders merely altered the  $\kappa$ .<sup>15</sup> The phonon linewidths and phonon density of states were merely altered as well.<sup>15</sup> On the other hand, the previous MD results on  $\alpha$ - and  $\beta\text{-Si}_3\text{N}_4$  presented that the different stacking orders in these phases altered the  $\kappa$  largely. This has not been explained through their phonon properties. It is interesting to investigate this based on the first principles anharmonic phonon calculation.

In addition to the  $\alpha$  and  $\beta$  phases, a cubic spinel phase ( $\gamma\text{-Si}_3\text{N}_4$ ) is known to form upon compression and in-situ heating.<sup>16,17</sup> The reported transition pressures are scattered from 10 to 36 GPa depending on the experimental conditions.<sup>18</sup> The  $\gamma$  phase is experimentally quenched to atmospheric pressure and room temperature. Its thermal conductivity has not been experimentally reported; it has been estimated by the Slack model.<sup>19</sup>

The present study aims to qualitatively understand the lattice thermal conductivity tensors among the three  $\text{Si}_3\text{N}_4$  phases by means of the first principles approach. We calculate the  $\kappa$  of the  $\gamma$  phase as well, for systematic understanding. After the methodology section, we examine the validity of the present results first. Our calculated thermal properties are compared with the available experimental and theoretical references. Then we investigate the characteristic behaviors of the  $\kappa$  in detail on the basis of the phonon band structures and phonon linewidths.

## II. COMPUTATIONAL PROCEDURES

### A. Lattice thermal conductivity calculation

The lattice thermal conductivities were calculated by solving the linearized Boltzmann transport equation (LBTE) within the single-mode relaxation time approximation (single-mode RTA). The harmonic phonon states and lattice thermal conductivities were calculated with phonopy<sup>20</sup> and phono3py<sup>15</sup> software packages, respectively. We also tried the direct-solution of LBTE<sup>21</sup> and

leave its calculated  $\kappa$  values in the following section. The differences between the  $\kappa$  calculated by the single-mode RTA and the direct solution were found minor for our discussion. Therefore we limited our research to use the single-mode RTA to take advantage of its intuitive closed form of  $\kappa$ .

In the following sections, we denote a phonon mode by  $\lambda = (\mathbf{q}, p)$  with the set of the phonon wave vector  $\mathbf{q}$  and band index  $p$  and  $-\lambda \equiv (-\mathbf{q}, p)$ . The relaxation time due to phonon-phonon scattering was obtained as reciprocal of linewidth,  $\tau_{\lambda, \text{ph-ph}} = (2\Gamma_{\lambda})^{-1}$ , where the linewidth that we employed in this study is as follows:

$$\begin{aligned} \Gamma_{\lambda} = & \frac{18\pi}{\hbar^2} \sum_{\lambda' \lambda''} |\Phi_{-\lambda \lambda' \lambda''}|^2 \times \\ & \{(n_{\lambda'} + n_{\lambda''} + 1)\delta(\omega_{\lambda} - \omega_{\lambda'} - \omega_{\lambda''}) + \\ & (n_{\lambda'} - n_{\lambda''})[\delta(\omega_{\lambda} + \omega_{\lambda'} - \omega_{\lambda''}) - \delta(\omega_{\lambda} - \omega_{\lambda'} + \omega_{\lambda''})]\}. \end{aligned} \quad (1)$$

Here  $\omega_{\lambda}$  is the harmonic phonon frequency of the phonon mode  $\lambda$ ,  $n_{\lambda} = [\exp(\hbar\omega_{\lambda}/k_B T) - 1]^{-1}$  is the Bose-Einstein distribution at temperature  $T$ , and  $\Phi_{\lambda \lambda' \lambda''}$  denotes the three-phonon-scattering strength.  $\Phi_{\lambda \lambda' \lambda''}$  was obtained by usual coordinate transformation of third-order force constants from direct space to phonon space.<sup>15</sup> The second- and third-order real-space force constants were obtained from the *ab-initio* calculation, whose details are written in the next section.

In order to compare the more realistic results of the calculated  $\kappa$  with the experimental thermal conductivities, the isotopic scattering effect due to the natural isotope distribution was taken into account according to the second-order perturbation theory.<sup>22</sup> With the relaxation times of the phonon-phonon scattering and isotopic scattering,  $\tau_{\lambda, \text{ph-ph}}$  and  $\tau_{\lambda, \text{iso}}$ , the total relaxation time for a phonon mode was assumed to be  $1/\tau_{\lambda} = 1/\tau_{\lambda, \text{ph-ph}} + 1/\tau_{\lambda, \text{iso}}$ , according to Matthiessen's rule.

The available experimental thermal conductivities in the  $\text{Si}_3\text{N}_4$  system were measured on the polycrystalline samples and not measured from any single crystals. The conductivities measured at a polycrystalline area were affected by various lattice defects within it, such as grain boundaries, impurities, and vacancies, we crudely took them into account by a relaxation time  $\tau_{\lambda, \text{bs}} = L/|\mathbf{v}_{\lambda}|$  of a phonon boundary scattering model, where  $\mathbf{v}_{\lambda} = \nabla_{\mathbf{q}}\omega_{\lambda}$  is the group velocity and  $L$  a parameter regarding to the boundary mean free path. We consider  $\tau_{\lambda, \text{bs}}$  as a variable parameter and partly include it to  $\kappa$  according to Matthiessen's rule.

The closed form of  $\kappa$  within RTA was obtained via

$$\kappa(T) = \frac{1}{N_{\mathbf{q}}\Omega} \sum_{\lambda} \tau_{\lambda}(T) \mathbf{v}_{\lambda} \otimes \mathbf{v}_{\lambda} c_{\lambda}(T), \quad (2)$$

where  $N_{\mathbf{q}}$  is the number of  $\mathbf{q}$ -points,  $\Omega$  is the unit cell volume, and  $c_{\lambda}$  is the mode heat capacity. To analyze  $\kappa$  in

detail, we calculate the cumulative thermal conductivity:

$$\kappa^c(\omega) = \frac{1}{N_{\mathbf{q}}\Omega} \int_0^\omega \sum_\lambda \tau_\lambda(T) \mathbf{v}_\lambda \otimes \mathbf{v}_\lambda c_\lambda(T) \delta(\omega' - \omega) d\omega', \quad (3)$$

and its derivative  $\frac{\partial \kappa^c(\omega)}{\partial \omega}$  to see the phonon mode contributions to  $\kappa$ .

## B. Computational details

The force constants were calculated using the first-principles projector augmented wave method<sup>23</sup> (VASP code<sup>24–26</sup>). The generalized gradient approximation (GGA) parameterized by Perdew, Burke, and Ernzerhof<sup>27</sup> was used for the exchange correlation potential. A plane wave energy cutoff of 500 eV was employed. The crystal structures were optimized until the residual forces acting on the constituent atoms were less than  $10^{-6}$  eV/Å. The structural optimization was firstly performed for a temperature of 0 K and 0 GPa. Here the temperature and pressure were considered only for the electronic system and the zero point lattice vibration was not taken into account. The calculated lattice parameters were  $a = 7.808$  Å and  $c = 5.659$  Å for the  $\alpha$  phase,  $a = 7.660$  Å and  $c = 2.925$  Å for the  $\beta$  phase, and  $a = 7.787$  Å for the  $\gamma$  phase, which agree with the experimental data<sup>7,8,28</sup> within +0.7 % errors. The lattice volume optimized with the local density approximation (LDA)<sup>29</sup> for the exchange correlation potential was, for  $\beta$ -Si<sub>3</sub>N<sub>4</sub>, 3 % smaller than the volume with GGA, which is a typical volume contraction of LDA. The  $\kappa$  calculated with LDA was larger by 2.6 % than the  $\kappa$  with GGA. For our discussion, this difference is enough small, therefore the impact of choice of exchange correlation potential is considered to be minor in our study.

The force constants were calculated by the finite difference approach<sup>30</sup>. For this calculation, we adopted the following supercells: The  $1 \times 1 \times 2$ ,  $1 \times 1 \times 3$ , and  $1 \times 1 \times 1$  supercells of the conventional unit cells for the third-order force constants of  $\alpha$ ,  $\beta$ , and  $\gamma$ -Si<sub>3</sub>N<sub>4</sub>, respectively, and the  $3 \times 3 \times 4$ ,  $3 \times 3 \times 8$  and  $2 \times 2 \times 2$  for the second-order force constants. The length of the induced atomic displacements was set to 0.03 Å. Table I shows the  $\kappa$  calculated with several different sets of the supercells, indicating that our calculated  $\kappa$  is reasonably converging with respect to the size of the supercells.

Uniform  $\mathbf{k}$ -point sampling meshes of  $4 \times 4 \times 2$ ,  $4 \times 4 \times 3$ , and  $3 \times 3 \times 3$  were used for the third-order force constants of the  $\alpha$ ,  $\beta$ , and  $\gamma$  phases. For the  $\alpha$  and  $\beta$  phases the center of the  $a^*b^*$  plane was sampled while the center on the  $c^*$ -axis was not. For the  $\gamma$  phase, non-Γ center mesh was used. For the second-order force constants, the Γ-point was only sampled for the  $\alpha$  and  $\beta$  phase and the only one  $\mathbf{k} = (0.5, 0.5, 0.5)$  point was sampled for the  $\gamma$  phase. The  $\mathbf{q}$ -point sampling meshes of  $10 \times 10 \times 14$ ,

TABLE I. Calculated lattice thermal conductivities of  $\alpha$ -,  $\beta$ -, and  $\gamma$ -Si<sub>3</sub>N<sub>4</sub> (WK<sup>-1</sup>m<sup>-1</sup>) at 300 K with respect to several combinations of supercell sizes.

Phase	Supercell (# of atoms)		LTC	
	3 <sup>rd</sup> force constants	2 <sup>nd</sup> force constants	$xx$	$zz$
$\alpha$	1 $\times$ 1 $\times$ 1 (28)	1 $\times$ 1 $\times$ 1 (28)	37	57
	1 $\times$ 1 $\times$ 2 (56)	1 $\times$ 1 $\times$ 2 (56)	41	79
	1 $\times$ 1 $\times$ 1 (28)	2 $\times$ 2 $\times$ 2 (224)	55	81
	1 $\times$ 1 $\times$ 2 (56)	2 $\times$ 2 $\times$ 2 (224)	67	95
	1 $\times$ 1 $\times$ 2 (56)	2 $\times$ 2 $\times$ 3 (336)	68	97
	1 $\times$ 1 $\times$ 2 (56)	3 $\times$ 3 $\times$ 4 (1008)	68	100
$\beta$	1 $\times$ 1 $\times$ 2 (28)	1 $\times$ 1 $\times$ 2 (28)	44	173
	1 $\times$ 1 $\times$ 2 (28)	2 $\times$ 2 $\times$ 4 (224)	76	208
	1 $\times$ 1 $\times$ 3 (42)	2 $\times$ 2 $\times$ 4 (224)	71	194
	1 $\times$ 1 $\times$ 3 (42)	2 $\times$ 2 $\times$ 5 (280)	72	196
	1 $\times$ 1 $\times$ 3 (42)	3 $\times$ 3 $\times$ 8 (1008)	73	199
$\gamma$	1 $\times$ 1 $\times$ 1 (56)	1 $\times$ 1 $\times$ 1 (56)	72	
	1 $\times$ 1 $\times$ 1 (56)	2 $\times$ 2 $\times$ 2 (448)	77	
	1 $\times$ 1 $\times$ 1 (56)	3 $\times$ 3 $\times$ 3 (56)	79	

$10 \times 10 \times 26$ , and  $12 \times 12 \times 12$  were used to calculate  $\kappa$  in Eq. (2) for the  $\alpha$ ,  $\beta$ , and  $\gamma$  phases.

Non-analytical term correction<sup>31</sup> was applied to the second-order force constants to take into account the long range Coulomb forces present in ionic crystals. For the correction, static dielectric constants and Born effective charges were calculated by using the density functional perturbation theory as implemented in the VASP code<sup>32,33</sup>.

We examined the effect of thermal expansion on  $\kappa$ . For this, we calculated the  $\kappa$  with the crystal structures which were optimized for several finite temperatures within the quasi-harmonic approximation (QHA)<sup>34</sup>. These  $\kappa$  were different from the  $\kappa$  for the corresponding temperatures, calculated with the structure which was initially optimized for 0 K. We consider these differences as the effect of thermal expansion. We calculated the differences between the  $\beta$ -Si<sub>3</sub>N<sub>4</sub> structures for  $T=300, 600, 900, 1200$ , and,  $1500$  K. The differences were found within 1 %, similar to the case of Si and Ge<sup>35</sup>. For the present study, these differences are negligible and we adopted the  $\kappa$  calculated with the structure which was initially optimized for 0 K.

In addition, we calculated the volumetric thermal expansion coefficients. Their comparison with the experimental coefficients is useful to validate the present thermal conductivity calculation, because the thermal expansion is originated from the anharmonicity of the interatomic potential as well as  $\kappa$ . The calculated coefficients of the  $\alpha$  and  $\beta$  phases were  $4.31 \times 10^{-6}$  and  $4.19 \times 10^{-6}$  K<sup>-1</sup> for 300 K, while the experimental values<sup>36</sup> are  $3.75 \times 10^{-6}$  and  $3.55 \times 10^{-6}$  K<sup>-1</sup>. The calculation reproduced the experimental tendency where the  $\alpha$  phase has a slightly larger thermal expansion coefficient

than the  $\beta$  phase. This supports that the present calculation enables us to qualitatively compare the calculated  $\kappa$  among the  $\text{Si}_3\text{N}_4$  phases.

In order to compare the microscopic phonon properties among the three phases at the same conditions, those results calculated at 0 GPa are shown and discussed. For the  $\gamma$  phase, this means that we assume the condition of a virtually quenched  $\gamma$  phase at 0 GPa from the high pressure. To examine the analytical continuity of the properties with respect to pressures, we calculated  $\kappa$  of the  $\gamma$  phase at 10, 20, and 40 GPa as shown in Fig. 9. The phenomenological behaviour of linear dependence of  $\kappa$  with respect to pressure was reproduced as similar to Ref. 37. The slope was  $2.89 \text{ Wm}^{-1}\text{K}^{-1}\text{GPa}^{-1}$  for the  $\gamma$  phase. By this dependence, we consider that the microscopic values are also varied smoothly with the pressure and those at 0 GPa are valuable to compare with the  $\alpha$  and  $\beta$  phases.

### C. Direct solution of LBTE

The merit to employ the single-mode RTA for thermal conductivity calculation is the closed form, by which we can intuitively understand the qualitative character of  $\kappa$  in terms of the relaxation time and group velocity. The microscopic understanding of the full solution of LBTE is still under the development<sup>38</sup> and the microscopic picture based on collective phonons<sup>39</sup> will require more complicated investigation.

It is known that the single-mode RTA solution of LBTE often underestimates the full solution.<sup>35,40</sup> To check the underestimation, we calculated  $\kappa$  of the  $\alpha$  and  $\beta$  phases by a direct solution of LBTE<sup>21</sup>, which is one of the methods of LBTE full solutions. Their  $\kappa_{xx}$  and  $\kappa_{zz}$  without the isotope effect were 69 and  $102 \text{ Wm}^{-1}\text{K}^{-1}$  for the  $\alpha$  phase and 76 and  $238 \text{ Wm}^{-1}\text{K}^{-1}$  for the  $\beta$  phase, respectively, while the corresponding single-mode RTA values were 70 and  $102 \text{ Wm}^{-1}\text{K}^{-1}$  for the  $\alpha$  phase and 76 and  $210 \text{ Wm}^{-1}\text{K}^{-1}$  for the  $\beta$  phase. The  $\kappa_{zz}$  of the direct solution in the  $\beta$  phase was 13 % larger than that of the single-mode RTA solution. Since the differences in  $\kappa$  between the LBTE solutions are not significant, we expect the physics on those lattice thermal conductivities is well understood within the single-mode RTA in the current level of our interest. Therefore, we discuss the lattice thermal conductivities calculated by the single-mode RTA solution.

## III. RESULTS AND DISCUSSION

### A. Lattice thermal conductivities

Table II shows the present results of the  $\kappa$  for 300 K.  $\beta\text{-Si}_3\text{N}_4$  has a markedly more anisotropic  $\kappa$  than  $\alpha\text{-Si}_3\text{N}_4$ . The directional averages  $\sum_i \kappa_{ii}/3$  are 79, 115, and 77  $\text{Wm}^{-1}\text{K}^{-1}$  for the  $\alpha$ ,  $\beta$ , and  $\gamma$  phases, respectively. The

TABLE II. Calculated thermal conductivities of  $\alpha\text{-Si}_3\text{N}_4$  (trigonal),  $\beta\text{-Si}_3\text{N}_4$  (trigonal), and  $\gamma\text{-Si}_3\text{N}_4$  (cubic) at 300 K, compared with the experimental and theoretical reference data. Theoretical bulk moduli  $B$  in units of GPa, calculated by the authors by using the present band method, are additionally presented in the fourth column.

	This work			Ref. Theo.		Ref. Expt.		
	$\kappa_{xx}$	$\kappa_{zz}$	$B$	$\kappa$	$\kappa_{xx}$	$\kappa_{zz}$	$\kappa_{xx}$	$\kappa_{zz}$
$\alpha\text{-Si}_3\text{N}_4$	68	100	224	70 <sup>a</sup>	105 <sup>b</sup>	225 <sup>b</sup>	-	-
$\beta\text{-Si}_3\text{N}_4$	73	199	237	250 <sup>a</sup>	170 <sup>b</sup>	450 <sup>b</sup>	69 <sup>c</sup>	180 <sup>c</sup>
$\gamma\text{-Si}_3\text{N}_4$	77	-	296	80 <sup>a</sup>	-	-	-	-

<sup>a</sup> Ref. 19, Slack model.

<sup>b</sup> Ref. 12, molecular dynamics (Green-Kubo).

<sup>c</sup> Ref. 13, single crystalline grains of poly-crystals.

value of the  $\gamma$  phase is similar to that of the  $\alpha$  phase, in spite of comparatively large difference among the bulk moduli ( $B$ ) that are also shown in Table II.

Table II also lists the previously reported experimental<sup>13</sup> and theoretical<sup>12</sup>  $\kappa$  for the references. The theoretical results<sup>19</sup> of the Slack model, which do not include the anisotropy in  $\kappa$ , are shown as  $\kappa$  in Table II. For the  $\beta$  phase, compared to the  $\kappa$  of the molecular dynamics<sup>12</sup>, our  $\kappa$  agrees better with the experimental  $\kappa$ . Also, compared to the  $\kappa$  of the Slack model, our directional average  $\sum_i \kappa_{ii}/3$  is much closer to the experimental average.

Fig. 2 shows the theoretical  $\kappa$  of the  $\alpha$  and  $\beta$  phases as a function of  $T$ , together with the reference experimental data<sup>5,11</sup>. The experimental thermal conductivities for a series of temperatures were measured on the polycrystalline sample areas by the laser flash method. These thermal conductivities (denoted as  $\kappa_{\text{polycrystal}}$ ) cannot be directly compared with the calculated intrinsic  $\kappa$  because they largely depended on the microstructure of the samples: They were deviated from the simple directional averages of the intrinsic  $\kappa_{ii}$ , depending on the shapes of the crystal grains. We treated this effect by using a parameter  $0 \leq w \leq 1$  and fitting the quantities of  $w\kappa_{xx} + (1-w)\kappa_{zz}$  to the experimental  $\kappa_{\text{polycrystal}}$  by the least squares method. We consider these as theoretical  $\kappa_{\text{polycrystal}}$ .

In Fig. 2, the  $\kappa_{ii}$  calculated without  $\tau_{\lambda,\text{bs}}$  are nearly proportional to  $T^{-1}$  because  $n_\lambda$  in Eq. (1) can be reduced to  $\exp(-\hbar\omega_\lambda/k_B T)$ . In Fig. 2-a, the experimental  $\kappa_{\text{polycrystal}}$  of a chemically vapor-deposited  $\alpha\text{-Si}_3\text{N}_4$  sample<sup>11</sup> is not proportional to  $T^{-1}$  and intersects the theoretical  $\kappa_{ii}$ . Thus no value of  $w$  adjusts the theoretical  $\kappa_{\text{polycrystal}}$  to the experimental  $\kappa_{\text{polycrystal}}$ . The full solution of LBTE would negligibly cure the disagreement. Including the simple phonon lifetime of boundary scattering,  $\tau_{\lambda,\text{bs}} = L/|\mathbf{v}_\lambda|$ , into the total phonon lifetime according to Matthiessen's rule, could not explain the discrepancy as well. A  $L$  value of 0.6  $\mu\text{m}$ , which was much smaller than the experimental grain size<sup>11</sup> of 10  $\mu\text{m}$ , decreased the theoretical  $\kappa_{ii}$  in the low temperature side toward the experimental values, but kept the

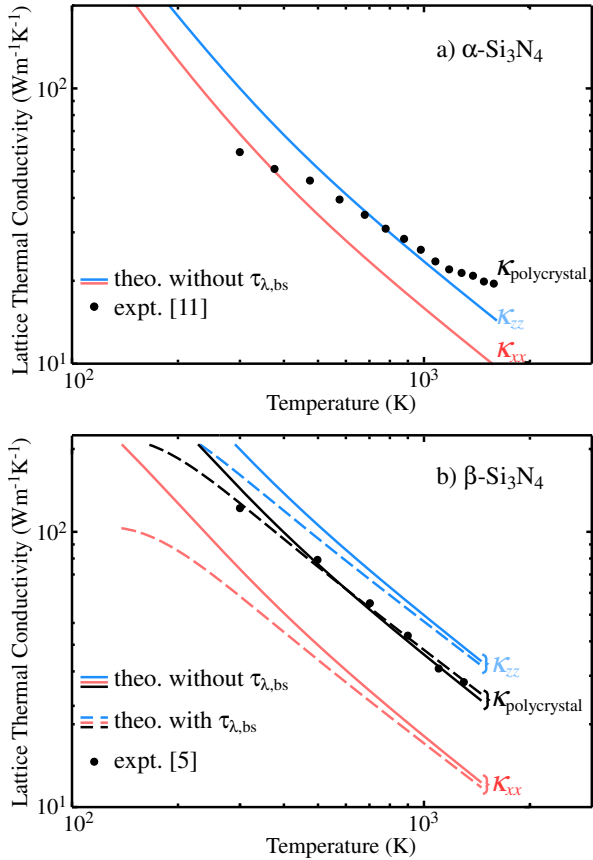


FIG. 2. (color online) Temperature dependences of thermal conductivities for  $\alpha$ - and  $\beta$ - $\text{Si}_3\text{N}_4$ . For  $\beta$ - $\text{Si}_3\text{N}_4$ , theoretical conductivities with the boundary scattering effect are shown by broken lines. Theoretical  $\kappa_{\text{polycrystal}}$  (see in text) for the  $\beta$ - $\text{Si}_3\text{N}_4$  sample are also shown to be compared with the experimental conductivities.

$\kappa_{ii}$  in the high temperature side severely smaller than the experimental values. At present, the reason for the discrepancy between the theoretical and experimental behaviors is unclear. Although the crystal structure of the experimental sample was characterized as  $\alpha$ - $\text{Si}_3\text{N}_4$ , significant lattice defects existed in the sample as pointed out by Hirosaki *et al.*<sup>12</sup> and the simple phonon boundary scattering model may fail to describe their effects on the  $\kappa_{\text{polycrystal}}$ .

For the  $\beta$  phase, the experimental  $\kappa_{\text{polycrystal}}$  are located in-between the theoretical  $\kappa_{xx}$  and  $\kappa_{zz}$ , being nearly proportional to  $T^{-1}$ . Simple directional averages of the theoretical  $\kappa_{ii}$  slightly underestimate these experimental values. This is understood from the fact that the microstructure was controlled to increase the  $\kappa_{\text{polycrystal}}$ , and the crystalline grains were selectively grown along the  $c$  axis of the most conductive direction.<sup>5</sup> The theoretical  $\kappa_{\text{polycrystal}}$  were fit well with  $w = 0.44$  to the experimental. For the effects of lattice defects most of which were grain boundaries, we included  $\tau_{\lambda,\text{bs}}$  with  $L = 0.6 \mu\text{m}$  to further fit the theoretical curve ( $w = 0.33$ ) to the

experimental data. The  $L$  value is slightly smaller than the average grain size<sup>5</sup> of  $2 \mu\text{m}$  in the experiment.

## B. Dispersion curves

Figure 3 shows the phonon band diagrams of the three  $\text{Si}_3\text{N}_4$  phases. The entire band diagrams are almost identical to those reported earlier<sup>18,41</sup>. However, here we investigate the gradients of  $\omega_\lambda$ , that is, the group velocities projected on the high-symmetry paths. We especially focus on their anisotropy in the  $\alpha$  and  $\beta$  phases. This was not investigated by the previous works.

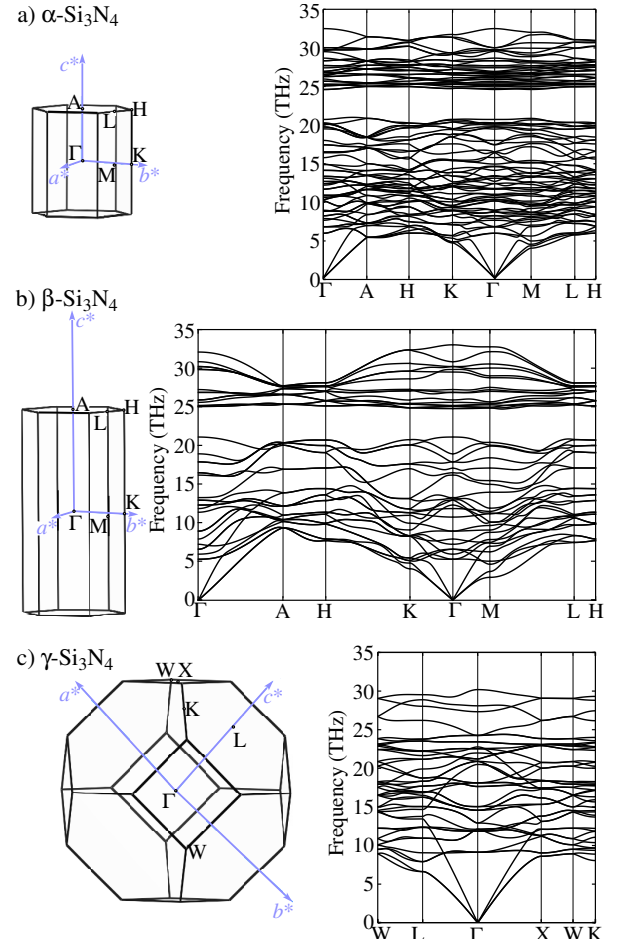


FIG. 3. (color online) Brillouin-zones (left) and calculated phonon band diagrams (right) for three  $\text{Si}_3\text{N}_4$  phases.

In Fig.3-b, the acoustic phonon branches in the  $\beta$  phase increase their  $\omega_\lambda$  much more from  $\Gamma$  to  $A$  than from  $\Gamma$  to  $K$  or  $\Gamma$  to  $M$ . In Fig.3-a of the  $\alpha$  phase, the corresponding  $\omega_\lambda$  increase similarly among these paths. This difference is due to the  $\Gamma$ - $A$  path lengths. The  $\beta$  phase has an approximately twice longer path than the  $\alpha$  phase; the lattice constant  $c$  of the  $\beta$  phase is nearly half that of the  $\alpha$  phase, owing to the different stacking manners of the basal layer structures. The anisotropic increments

of  $\omega_\lambda$  indicate the anisotropic  $\mathbf{v}_\lambda$ . This will be investigated further in the following sections. Normally, optical phonon branches are flat; however, the  $\beta$  phase shows significantly large gradients of  $\omega_\lambda$  in the low frequency optical phonon branches. This indicates that the  $\mathbf{v}_\lambda$  of these phonon modes are large.

In the  $\gamma$  phase, the acoustic phonon branches show significantly linear dispersion-relations. Their gradients are large, reflecting the large  $B$  of the  $\gamma$  phase.

### C. $\omega_\lambda$ contour map on reciprocal plane

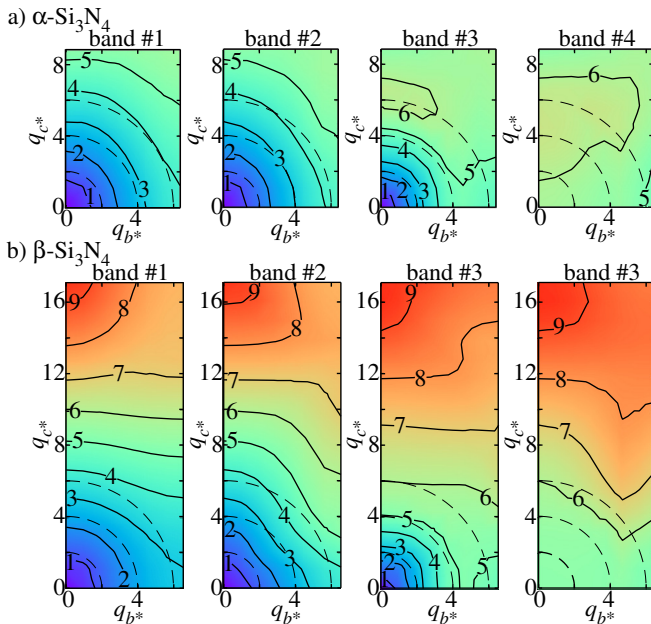


FIG. 4. (color online) Contour maps of phonon frequency (THz) on the  $b^*c^*$  planes of Brillouin-zones. The coordination in the reciprocal plane are in units of  $10^{-2} \text{ \AA}^{-1}$ . The maps for the four lowest-frequency phonon modes are shown. The frequency landscapes are formed by simply connecting the frequencies of the same band indices, assigned by ascending order of frequency at the respective  $\mathbf{q}$  points.

We investigate the anisotropy in the  $\mathbf{v}_\lambda$  by using another geometry, that is, a cross-section of the Brillouin-zone. Fig. 4 shows contour maps of  $\omega_\lambda$  on the  $b^*c^*$  plane. We show the maps for the four lowest-frequency bands, because they contribute significantly to the  $\kappa$ , which will be confirmed in the next section. There were negligible differences between the distributions on the  $b^*c^*$  plane and the other planes containing the  $c^*$  axis. Thus we select the  $b^*c^*$  plane as a representative. In the  $\alpha$  phase, the  $\omega_\lambda$  distributions and thus  $\mathbf{v}_\lambda$  are nearly isotropic. In the  $\beta$  phase, the contours are rather parallel to the  $b^*$  axis and thus the  $\mathbf{v}_\lambda$  tend to orient toward the  $c^*$  axis direction. This confirms the large anisotropy of the  $\mathbf{v}_\lambda$  in the  $\beta$  phase for the acoustic and low-frequency optical phonon branches.

### D. Frequency-distributions of phonon properties

We have investigated in the previous two sections the anisotropy in the  $\mathbf{v}_\lambda$ , which can explain the anisotropy in the  $\kappa$ . Here we more completely investigate the  $\kappa$  based on the phonon properties composing the RTA closed form in Eqs. (2,3).

The mode heat capacity,  $c_\lambda$ , in Eqs. (2,3) is approximately constant for 300 K and disregarded in the following, for simplicity. Assuming  $\tau_\lambda$  and  $\mathbf{v}_\lambda$  constant, then the  $\omega$ -derivatives of the diagonal components in Eq. (3),  $d\kappa_{ii}^c/d\omega$ , is proportional to phonon density of states (DOS)

$$g(\omega) = \frac{1}{N_q \Omega} \sum_\lambda \delta(\omega - \omega_\lambda). \quad (4)$$

In this context  $g(\omega)$  can be viewed as frequency distributions of heat carrier density. Alternatively, assuming only  $\tau_\lambda$  constant, then  $d\kappa^c/d\omega$  is proportional to

$$\mathbf{h}(\omega) = \frac{1}{N_q \Omega} \sum_\lambda \mathbf{v}_\lambda \otimes \mathbf{v}_\lambda \delta(\omega - \omega_\lambda), \quad (5)$$

which informs the impacts of both of the  $\mathbf{v}_\lambda$  and heat carrier density.  $g(\omega)$ ,  $\mathbf{h}(\omega)$ , and,  $\mathbf{k}^c(\omega)$  as well as  $d\kappa^c/d\omega$  are shown in Figs. 5-a, b, and, c, respectively. As for the frequency variation of  $\tau_{\lambda,ph-ph}$ , phonon linewidths are shown as scatter plots of  $(\Gamma_\lambda, \omega_\lambda)$  in Fig. 5-d. The effects of the isotope scattering and boundary scattering are not included in the  $\kappa^c$  and their derivative for consistency with  $\Gamma_\lambda$ .

Firstly, from Fig. 5-c, we find that, in the  $\alpha$ ,  $\beta$ , and  $\gamma$  phases, the phonon modes upto  $\sim 6$ ,  $\sim 12$  and  $\sim 10$  THz largely contribute to the respective  $\kappa$ . We confirm that the  $\omega_\lambda$  shown in Fig. 4 are smaller than these upper bounds and those bands significantly contribute to the  $\kappa$ .

Next, we compare the properties between the  $\alpha$  and  $\beta$  phases. Their linewidth distributions are qualitatively similar, except for a striking difference between 0-5 THz, which will be examined later. The markedly different  $d\kappa_{ii}^c/d\omega$  between the two phases are therefore ascribed to the corresponding  $h_{ii}$ . Moreover, because the  $g(\omega)$  are also similar between the two phases, the  $\mathbf{v}_\lambda$  alone accounts for the different behaviors of the  $d\kappa_{ii}^c/d\omega$ .

The  $\gamma$  phase has much different  $g(\omega)$ ,  $\mathbf{h}(\omega)$ , and,  $\Gamma_\lambda$  from the others as expected from the large differences in the crystal structure. The most significant difference is in its  $\Gamma_\lambda$ . For  $\omega \lesssim 10$ , the linewidths are approximately twice larger than those of the other phases. We will examine this details later. As a result of the large  $\Gamma_\lambda$  the  $d\kappa_{xx}^c/d\omega$  is not so large. Since the acoustic phonon branches extends to rather high frequencies, as we have examined in the band diagram, the  $d\kappa_{xx}^c/d\omega$  occasionally resembles to that of the  $\beta$  phase.

It is still curious that  $\Gamma_\lambda$  are similar between the  $\alpha$  and  $\beta$  phases although  $\mathbf{v}_\lambda$  show marked differences. In analogy to Lindsay *et al.*<sup>42</sup>, we can say that  $\Gamma_\lambda$  in the present

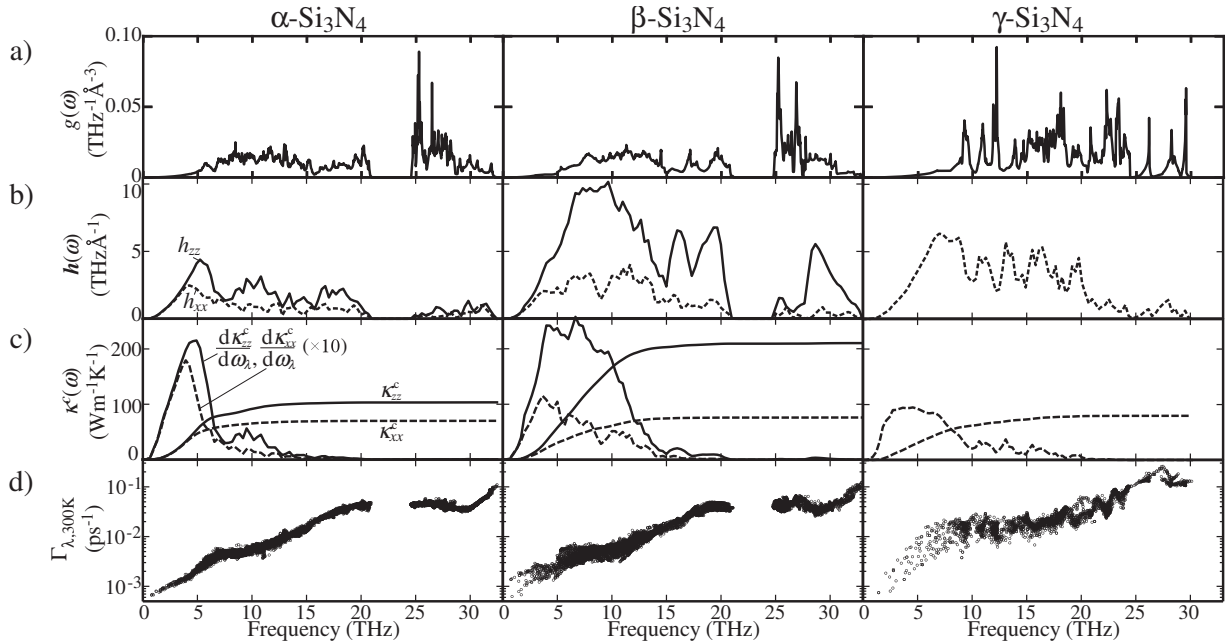


FIG. 5. (color online) Microscopic phonon properties of three  $\text{Si}_3\text{N}_4$  phases. DOS (a), Cumulative thermal conductivity  $\kappa^c$  and its derivative (b), weighted DOS with  $v_{\lambda,i}^2$  (c), and linewidth  $\Gamma_\lambda$  (d).

form depends on the phase space for the available two phonons,  $\{\lambda', \lambda''\}$ , but it also depends on  $|\Phi_{\lambda\lambda'\lambda''}|^2$ : We examine these terms one-by-one. A distribution of two-phonon configurations is represented as a joint density of states (JDOS),  $D_2(\mathbf{q}, \omega)$ ,

$$D_2(\mathbf{q}, \omega) = D_2^{(1)}(\mathbf{q}, \omega) + D_2^{(2)}(\mathbf{q}, \omega) \quad (6)$$

where

$$\begin{aligned} D_2^{(1)} &= \frac{1}{N_{\mathbf{q}} Z^2} \sum_{\lambda' \lambda''} \Delta(-\mathbf{q} + \mathbf{q}' + \mathbf{q}'') \\ &\times [\delta(\omega + \omega_{\lambda'} - \omega_{\lambda''}) + \delta(\omega - \omega_{\lambda'} + \omega_{\lambda''})], \\ D_2^{(2)} &= \frac{1}{N_{\mathbf{q}} Z^2} \sum_{\lambda' \lambda''} \Delta(-\mathbf{q} + \mathbf{q}' + \mathbf{q}'') \\ &\times \delta(\omega - \omega_{\lambda'} - \omega_{\lambda''}), \end{aligned}$$

with  $\Delta(\mathbf{x})$  giving 1 if  $\mathbf{x}$  is a reciprocal lattice vector and otherwise zero.  $Z$  is the number of formula units in the unit cell. In more rigorous study, instead of  $D_2^{(1)}$  and  $D_2^{(2)}$  terms, we should employ  $(n_{\lambda'} + n_{\lambda''} + 1)$ - and  $(n_{\lambda'} - n_{\lambda''})$ -weighted JDOS terms. We firstly employ the JDOS in Eq. (6) to intuitively examine the similarity between the  $\Gamma_\lambda$  of the  $\alpha$  and  $\beta$  phases. The weighted JDOS (WJDOS) will be briefly shown later including that of the  $\gamma$  phase.

Fig. 6 shows frequency-functions of JDOS at several different  $\mathbf{q}$ -points. They have very weak  $\mathbf{q}$ -point dependences. At the low frequency region upto  $\simeq 10$  THz  $D_2^{(1)}$  is dominant between the two terms. The  $D_2^{(1)}$  are similar between the phases. In the present  $\text{Si}_3\text{N}_4$  system, the phonon modes in the acoustic and low-frequency optical branches, which largely contribute to the  $\kappa$ , are

much fewer than the other phonon modes. The JDOS are mainly determined by these majorities, even if the frequency is close to the  $\omega_\lambda$  of the acoustic and low-frequency optical phonon modes. As in the band diagrams, the branches of the majorities are rather flat. Thus we can approximately disregard in Eq. (6) the dependences of the  $\omega_{\lambda'}$  and  $\omega_{\lambda''}$  on the  $\mathbf{q}'$  and  $\mathbf{q}''$ . In this case  $D_2^{(1)}$  basically corresponds to the half part ( $\omega \geq 0$ ) of the auto-correlation function of the DOS. The DOS for both of the  $\alpha$  and  $\beta$  phases in Fig. 5-a have a frequency gap. The  $D_2^{(1)}$  reflect this DOS feature, dropping suddenly around 0 THz and showing a small shoulder around 5 THz. This shoulder frequency corresponds to the width of the gap. Because the gap is originated from the local modes of the planer  $\text{NSi}_3$  composing each of the  $\alpha$  and  $\beta$  crystal structures,<sup>41</sup> the  $D_2^{(1)}$  are similar in these phases.

The WJDOS,  $N_2(\omega, \mathbf{q})$ , are shown in Fig. 7. For the comparison among the three phases, we only show the frequency distributions at  $\mathbf{q} = (0, 0, 0)$  because the  $\mathbf{q}$  dependences of the WJDOS were as weak as JDOS. The terms corresponding to  $D_2^{(1)}$  and  $D_2^{(2)}$  are denoted as  $N_2^{(1)}$  and  $N_2^{(2)}$ . The weighting factors reduce the  $N_2^{(1)}$  near 0 THz and enhance the  $N_2^{(2)}$  in the high frequency range.  $N_2^{(1)}$  are dominant in the low frequency range of  $\omega \lesssim 10$  THz. These  $N_2^{(1)}$  are similar among the three phases.

As for  $|\Phi_{\lambda\lambda'\lambda''}|^2$ , in Table. III, they are averaged over two kinds of frequency ranges of 0–15 or 0–30 THz for  $\omega_\lambda$  and all indices in  $\lambda'$  and  $\lambda''$ . The averages are very similar values between the  $\alpha$  and  $\beta$  phases. With

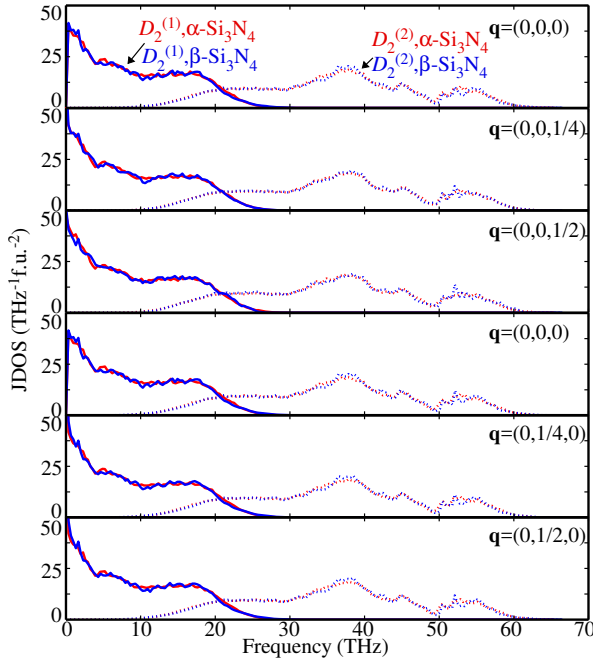


FIG. 6. (color online) JDOS of  $\alpha$ - and  $\beta$ - $\text{Si}_3\text{N}_4$  at different  $\mathbf{q}$  points. The first and forth rows are JDOS at the same  $\Gamma$ -point but calculated with the polarization for non-analytic term correction set along  $c^*$  and  $b^*$ , respectively.

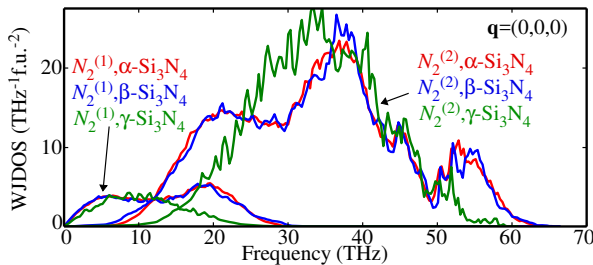


FIG. 7. (color online) Comparison of WJDOS at  $\mathbf{q} = (0,0,0)$  for 300 K among the three phases.

the similar impacts of the (W)JDOS and  $|\Phi_{\lambda\lambda'\lambda''}|^2$ , the linewidth distributions are similar. For the  $\gamma$  phase, the large  $|\Phi_{\lambda\lambda'\lambda''}|^2$  attribute to the large linewidths. We set the frequency ranges for  $\omega_\lambda$  so that the lower frequency range approximately corresponds to the range where the phonon modes largely contribute to the  $\kappa$ . A small change in the frequency ranges by a few THz did not change the qualitative characters of the averages.

Finally, we examine the exceptional, but striking difference in linewidth distributions between the  $\alpha$  and  $\beta$  phases: In the  $\alpha$  phase,  $\Gamma_\lambda$  below 5 THz are aligned on a single smooth line, while in the  $\beta$  phase, they are scattered roughly on two branches. This difference is investigated with directions of the atomic vibrations of the phonon modes. Fig. 8 enlarges the  $(\Gamma_\lambda, \omega_\lambda)$  plots in this frequency range. In Fig. 8-a, the  $\Gamma_\lambda$  are classified using colors according to the sums of the squares of

TABLE III. Averages of  $\Phi_{\lambda\lambda'\lambda''}$  over frequency ranges of  $\omega_\lambda$  (0–15 and 0–35 THz) and all  $(\lambda', \lambda'')$ . The values are in units of  $10^{-9}$  eV $^2$ f.u. $^2$ .

Frequency Range (THz)	Phase		
	$\alpha$	$\beta$	$\gamma$
0–15	1.1	1.1	2.3
0–30	5.2	5.2	4.6

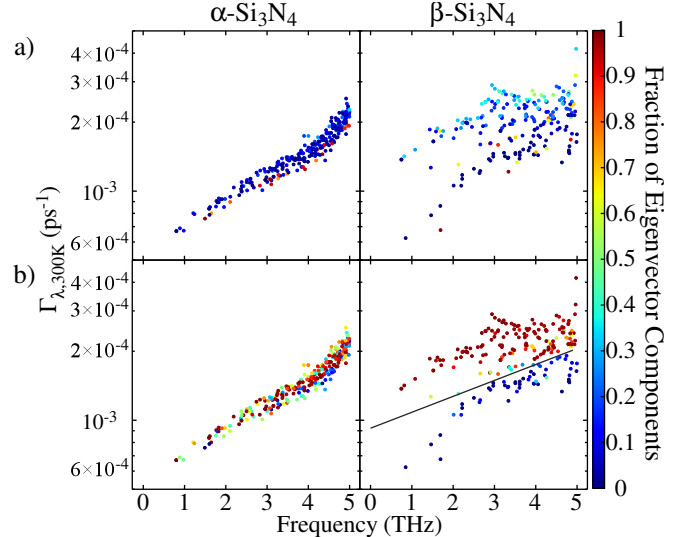


FIG. 8. (color online) Distribution of linewidths  $\omega_\lambda \leq 5$  THz with colors with respect to strengths of eigenvector components along  $\mathbf{q}$  (a) and on  $ab$  plane (b).

the eigenvector components along the  $\mathbf{q}$ ; the sum is 1 for a perfectly longitudinal wave. However, these sums show no clear contrast between the two branches in the  $\beta$  phase. Fig. 8-b shows the same plot as Fig. 8-a, but with colors according to the sums of the squares of the eigenvector components along the  $ab$  plane, which has 1 when the eigenvectors lie on the  $ab$  plane. There is a tendency in the  $\beta$  phase that  $\Gamma_\lambda$  are large for atomic vibrations along the  $ab$  plane. This means that the vibration modes along the  $ab$  plane, belonging to the acoustic phonon branches, are more easily scattered in the  $\beta$  phase, no matter whether they are longitudinal or transverse. For the panel of  $\beta$ - $\text{Si}_3\text{N}_4$  in Fig. 8-b, a straight line splits the phonon modes to two groups. The numbers of the phonon modes assigned to the larger and smaller  $\Gamma_\lambda$  groups are 157 and 58, whose ratio is confirmed close to the population ratio of the vibration modes along and out of the  $ab$  plane.

#### IV. SUMMARY

In the present study, we investigate the lattice thermal conductivities of the three  $\text{Si}_3\text{N}_4$  phases, by using the lattice dynamics based on the first principles interatomic

force constants. The main remarks are as follows:

1) In the  $\alpha$ - and  $\beta$ - $\text{Si}_3\text{N}_4$ , whose crystal structures are characterized by the stacking manners of the basal layer structures, which largely alter  $\kappa$ . This contrasts with the case of the zincblende and wurtzite structures in the previous study<sup>15</sup>. The  $\kappa$  of  $\alpha$ - $\text{Si}_3\text{N}_4$  is rather isotropic, while the  $\kappa_{zz}$  of the  $\beta$  phase is twice or more larger than the other  $\kappa_{ii}$  of the three phases.

2) In the  $\alpha$  phase, the acoustic mode phonons below 6 THz are the main heat carriers, while in the  $\beta$  phase, the phonons below 12 THz contribute to the  $\kappa$ . The group velocities alone largely depend on the stacking manners and qualitatively explain the behaviours of  $\kappa$ .

3) In the  $\gamma$  phase, the  $\kappa_{xx}$  is relatively small. The  $\kappa_{xx}^c$  is similar to that of  $\beta$ - $\text{Si}_3\text{N}_4$ . Its large  $|\Phi_{\lambda\lambda'\lambda''}|^2$  and acoustic phonon branches extending to high frequencies attribute to these characters.

In contrast to  $\alpha$ - and  $\beta$ - $\text{Si}_3\text{N}_4$ , in the case of the zincblende and wurtzite structures, the group velocities are suggested to be similar from their band structures<sup>15</sup>.

This results in marked difference in the relationship between the stacking manners and  $\kappa$ . The precise examination of  $\kappa$  based on the band structures is essential for systematic understanding of  $\kappa$  in a wide variety of crystal structures.

## ACKNOWLEDGMENTS

The present work was partly supported by Grants-in-Aid for Scientific Research of MEXT, Japan (Grant No. 15K14108 and ESISM (Elements Strategy Initiative for Structural Materials) of Kyoto University).

## Appendix A: Pressure dependence of lattice thermal conductivity of $\gamma$ -phase

\* k-tatsumi@imass.nagoya-u.ac.jp

- <sup>1</sup> G. Slack, Journal of Physics and Chemistry of Solids **34**, 321 (1973).
- <sup>2</sup> Y. Zhou, H. Hyuga, D. Kusano, Y.-i. Yoshizawa, and K. Hirao, Advanced Materials **23**, 4563 (2011).
- <sup>3</sup> K. Hirao, K. Watari, H. Hayashi, and M. Kitayama, MRS Bulletin **26**, 451 (2001).
- <sup>4</sup> K. Watari, Journal of the Ceramic Society of Japan **109**, S7 (2001).
- <sup>5</sup> N. Hirosaki, Y. Okamoto, M. Ando, F. Munakata, and Y. Akimune, Journal of the Ceramic Society of Japan **104**, 49 (1996).
- <sup>6</sup> F. L. Riley, Journal of the American Ceramic Society **83**, 245 (2000).
- <sup>7</sup> M. Yashima, Y. Ando, and Y. Tabira, The Journal of Physical Chemistry B **111**, 3609 (2007).
- <sup>8</sup> D. Du Boulay, N. Ishizawa, T. Atake, V. Streltsov, K. Furuya, and F. Munakata, Acta Crystallographica Section B: Structural Science **60**, 388 (2004).
- <sup>9</sup> S. Hampshire, H. Park, D. Thompson, and K. Jack, Nature **274**, 880 (1978).
- <sup>10</sup> T. Hahn, ed., International tables for crystallography, Vol. A (John Wiley & Sons, Inc., 2011).
- <sup>11</sup> T. Hirai, S. Hayashi, and K. Niihara, AM. CERAM. SOC. BULL. Am. Ceram. Soc. Bull. **57**, 1126 (1978).
- <sup>12</sup> N. Hirosaki, S. Ogata, C. Kocer, H. Kitagawa, and Y. Nakamura, Physical Review B **65**, 134110 (2002).
- <sup>13</sup> B. Li, L. Pottier, J. Roger, D. Fournier, K. Watari, and K. Hirao, Journal of the European Ceramic Society **19**, 1631 (1999).
- <sup>14</sup> R. Vashishta, R. K. Kalia, A. Nakano, and I. Ebbsö, Amorphous Insulators and Semiconductors, edited by M. F. Thorpe and M. I. Mitkova (Kluwer, 1996).
- <sup>15</sup> A. Togo, L. Chaput, and I. Tanaka, Physical Review B **91**, 094306 (2015).
- <sup>16</sup> A. Zerr, G. Miehe, G. Serghiou, M. Schwarz, E. Kroke, R. Riedel, H. Fueß, P. Kroll, and R. Boehler, Nature **400**, 340 (1999).

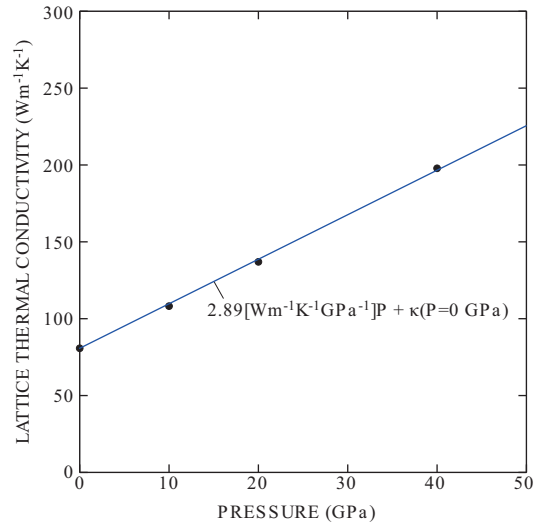


FIG. 9. (color online) Pressure dependence of lattice thermal conductivity of  $\gamma$ - $\text{Si}_3\text{N}_4$ .

- <sup>17</sup> Y. Zhang, A. Navrotsky, and T. Sekine, Journal of materials research **21**, 41 (2006).
- <sup>18</sup> B. Xu, J. Dong, P. F. McMillan, O. Shebanova, and A. Salamat, Physical Review B **84**, 014113 (2011).
- <sup>19</sup> D. Morelli and J. Heremans, Applied physics letters **81**, 5126 (2002).
- <sup>20</sup> A. Togo and I. Tanaka, Scripta Materialia **108**, 1 (2015).
- <sup>21</sup> L. Chaput, Physical review letters **110**, 265506 (2013).
- <sup>22</sup> S.-i. Tamura, Physical Review B **27**, 858 (1983).
- <sup>23</sup> P. E. Blöchl, Phys. Rev. B **50**, 17953 (1994).
- <sup>24</sup> G. Kresse and J. Furthmüller, Physical review B **54**, 11169 (1996).
- <sup>25</sup> G. Kresse, J. Non-Cryst. Solids **193**, 222 (1995).

- <sup>26</sup> D. J. Kresse, Georg, Phys. Rev. B **59**, 1758 (1999).
- <sup>27</sup> J. P. Perdew, K. Burke, and M. Ernzerhof, Phys. Rev. Lett. **77**, 3865 (1996).
- <sup>28</sup> W. Paszkowicz, R. Minikayev, P. Piszora, M. Knapp, C. Bähitz, J. Recio, M. Marques, P. Mori-Sánchez, L. Gerward, and J. Jiang, Phys. Rev. B **69**, 052103 (2004).
- <sup>29</sup> D. M. Ceperley and B. Alder, Physical Review Letters **45**, 566 (1980).
- <sup>30</sup> S. Wei and M. Chou, Physical review letters **69**, 2799 (1992).
- <sup>31</sup> Y. Wang, J. Wang, W. Wang, Z. Mei, S. Shang, L. Chen, and Z. Liu, J. Phys.: Condens. Matter **22**, 202201 (2010).
- <sup>32</sup> M. Gajdoš, G. Hummer, G. Kresse, J. Furthmüller, and B. F, Phys. Rev. B **73**, 045112 (2006).
- <sup>33</sup> X. Wu, D. Vanderbilt, and D. R. Hamann, Phys. Rev. B **72**, 035105 (2005).
- <sup>34</sup> M. T. Dove, *Introduction to lattice dynamics*, Vol. 4 (Cambridge university press, 1993) pp. 76–77.
- <sup>35</sup> A. Ward and D. Broido, Physical Review B **81**, 085205 (2010).
- <sup>36</sup> R. Minikayev, W. Paszkowicz, P. Piszora, M. Knapp, and C. Bähitz, “Thermal expansion of and silicon nitride,” (2007).
- <sup>37</sup> P. Andersson, Journal of Physics C: Solid State Physics **18**, 3943 (1985).
- <sup>38</sup> A. Cepellotti and N. Marzari, Physical Review X **6**, 041013 (2016).
- <sup>39</sup> R. J. Hardy, Physical Review B **2**, 1193 (1970).
- <sup>40</sup> S. Mukhopadhyay, L. Lindsay, and D. J. Singh, Scientific reports **6** (2016).
- <sup>41</sup> A. Kuwabara, K. Matsunaga, and I. Tanaka, Physical Review B **78**, 064104 (2008).
- <sup>42</sup> L. Lindsay and D. A. Broido, J. Phys.: Condens. Matter **20**, 165209 (2008).